CrossMark

A fourth order accuracy summation-by-parts finite difference scheme for acoustic reverse time migration in boundary-conforming grids

Ying Wang [a,b], Hui Zhou [a,*], Sanyi Yuan [a], Yameng Ye [c]

[a] *State Key Laboratory of Petroleum Resources and Prospecting, CNPC Key Lab of Geophysical Exploration, China University of Petroleum, 102249 Beijing, China*
[b] *State Key Laboratory of Acoustics, Institute of Acoustics, Chinese Academy of Sciences, 100190 Beijing, China*
[c] *School of Civil Engineering, Anhui Jianzhu University, China*

ARTICLE INFO

ABSTRACT

The fourth order accuracy finite difference scheme is known advantageous in reducing memory and improving efficiency. Summation-by-parts finite difference operator is a natural way for wavefield simulation in complicated domains containing surface topography and irregular interfaces. The application of summation-by-parts method guarantees the stability of numerical approximation for heterogeneous media on curvilinear grids. This paper extends the second order summation-by-parts finite difference method to the fourth order case for the discretization of acoustic wave equation and perfect matched layer in boundary-conforming grids. In particular, the implementation of the fourth order method for wavefield simulation and reverse time migration in complicated domains can significantly improve the efficiency and decrease the storage. The elliptic method is applied for boundary-conforming grid generation in complicated domains. Under such grids, the two-dimensional acoustic wave equation in second order displacement formulation is compactly reformulated for forward modeling and reverse time migration, and the symmetric and compact form of perfectly matched layers expressed in a curvilinear coordinate system are applied to suppress artificial reflections. The discretizations of the acoustic wave equation and perfectly matched layer formula are fourth and second order accuracy in space and time respectively, where the spatial discretization satisfies the principle of summation-by-parts and is stable. Numerical experiments are presented to compare the accuracy of the second with fourth order summation-by-parts finite difference methods and to evaluate the efficiency of reverse time migration by using these two methods. As well, comparisons are performed between the fourth order accuracy summation-by-parts finite difference method and central finite difference method to illustrate the stability superiority of summation-by-parts operators.

© 2016 Elsevier B.V. All rights reserved.

1. Introduction

Finite difference method (FDM) is flexible and easy to implement, it has been one of the most popular and successful numerical methods in seismic wavefield simulation for complex heterogeneous media. When structured meshes are readily generated, FDM can be the most efficient option for regions including many complex geometries of practical interest (Tarrass et al., 2011; Lan and Zhang, 2011, 2012; Del Rey Fernández et al., 2014). Applying a general form of transformation through elliptic partial differential equations, the elliptic method (Thompson et al., 1977a, 1977b; Thompson et al., 1985; Jeng and Liou, 1992; Kaul, 2003, 2010; Conti et al., 2005) provides a way to generate such structured boundary-conforming curvilinear grids. The surface

topography and irregular interfaces can be described precisely in boundary-conforming grids, which enables accurate modeling on realistic surface topography and makes FDM a very attractive alternative to finite element method (FEM) and pseudo-spectral method (PSM) (Petersson and Sjögreen, 2010; Sjögreen and Petersson, 2014). FEM is flexible in modeling complicated and irregular boundary conditions. However, FEM is computationally expensive and requires large amount of computer memory especially in the three-dimensional (3D) case (Komatitsch and Tromp, 1999; Liu et al., 2011; Guo and Wang, 2009; Guo et al., 2012; Sjögreen, 2012). PSM is also well adapted to handle a curved free surface efficiently. However, to fully utilize the high order PSM, unstructured high quality grid generation is needed, which is labor intensive and not easily automated. In addition, PSM leads to inaccuracies for models with strong heterogeneity or sharp boundaries (Fornberg, 1987; Kosloff et al., 1990).

The second order finite-difference scheme is a powerful tool in seismic modeling due to small storage and fast computation speed for the same grid points. Unfortunately, numerical dispersion affects the

---

* Corresponding author.
  E-mail address: huizhou@cup.edu.cn (H. Zhou).

performance of the second order FDM (Yang et al., 2012). As a result, high order spatially accurate finite difference schemes are required, because of their lower phase error (Mattsson, 2003). High order methods can produce more accurate results on coarser computational grids compared to low order ones, thus resulting in a decrease in the overall computational effort (Sherer and Scott, 2005). In particular, higher order finite-difference methods can offer a significant potential gain in computational efficiency (Sjögreen, 2012; Del Rey Fernández et al., 2014).

The main reason that low order FDMs are used in practical calculations is the difficulty to derive high accurate and stable operators in curvilinear grids. This fact has limited the use of high order finite difference method (HOFDM) in practical calculations to the small class of simple geometries (Del Rey Fernández et al., 2014). A natural way to obtain a stable and high order accurate approximation in the framework of HOFDM is to use summation-by-parts (SBP) operators. The SBP property refers to a discrete version of integration-by-parts, which leads to an attractive stability property (Nordstrom and Carpenter, 1998; Mattsson, 2003; Sherer and Scott, 2005; Hicken, 2012; Sjögreen and Petersson, 2012; Kozdon et al., 2013). This property ensures that the discretization can be generalized to curvilinear coordinates. Consequently, it is possible to account for realistic topography by constructing a boundary conforming curvilinear grid (Sjögreen and Petersson, 2014; Petersson and Sjögreen, 2015).

The research on HOFDM which satisfies SBP principle is popular due to the property that ensures the stability. Kress (2003) investigated the fourth order accuracy discretization in time and space for the wave equation in first order system formulation, but the discretization was based on staggered grid in space and was not applicable to curvilinear grids. Sjögreen (2012) implemented the finite difference scheme satisfying the SBP property for advection on the sphere, using the cube sphere discretization. Sjögreen and Petersson (2012) presented the fourth order accuracy SBP finite difference method (SBPFDM) for the elastic wave equation in second order formulation, where the boundary conditions were enforced through ghost points. Petersson and Sjögreen (2014) applied the super-grid approach combining with fourth order accuracy SBP operators to derive a stable and accurate numerical method for wave equations on unbounded domains. However, the effect of super-grid was not as ideal as perfectly matched layer (PML). Sjögreen and Petersson (2014) considered the inverse problem to estimate the parameters describing the source in a seismic event,

where the synthetic ground motions were obtained as the solution of a fourth order accuracy SBP finite difference approximation of the elastic wave equation in a heterogeneous isotropic material. Dovgilovich and Sofronov (2015) solved elastodynamic anisotropic problems described by the Navier wave equation in complex geometry based on the SBP approach, and non-reflecting boundary conditions were used. Petersson and Sjögreen (2015) extended the method for isotropic materials in Sjögreen and Petersson (2012) to general heterogeneous anisotropic materials on curvilinear grids, where the fourth order accuracy SBPFDM was applied for discretizing the anisotropic elastic wave equation in second order formulation and the super-grid far-field technique was used for truncating unbounded domains. Duru and Dunham (2016) solved the first order form of the 3D elastic wave equation by high order accuracy SBP finite difference operators for earthquake rupture dynamics on nonplanar faults embedded in geometrically complex, heterogeneous Earth models.

Previously, we have comprehensively applied the elliptic method in acoustic wave equation simulation, PMLs and reverse time migration (RTM) in boundary-conforming grids. The discretizations of the acoustic wave equation and PML formula were second order accuracy, where the spatial discretization satisfied the summation-by-parts principle (Wang et al., 2015). Here we generalize our technique to fourth order accuracy in space while the expression for the temporal derivative is retained second order accuracy, since using fourth order accuracy expression for the time derivative leads to an enormous increase in the computational effort (Mufti, 1990). The application of the fourth order SBPFDM in space can efficiently suppress the numerical dispersion, thus significantly improve the efficiency and decrease the storage in RTM. Lan et al. (2014) also did some work in the similar field, where the strategy of a flux-corrected transport (FCT) algorithm was incorporated in the RTM implementation to overcome the problem of numerical dispersion. However, the finite difference scheme is second-order accuracy, and more calculations, such as diffusion computation and offsetting diffusion, are needed in FCT-based FD algorithm.

This paper is organized as follows. First, a compactly reformulated acoustic wave equation is presented in boundary-conforming coordinates for wavefield simulation and RTM in regions with arbitrary surface and irregular interfaces, and the time domain PML formula of symmetric and compact form expressed in boundary-conforming coordinates is given. Then, the fourth order accuracy SBPFDM is used for discretization and the stability analysis of the scheme is given. Finally, three numerical examples with surface topography, irregular interfaces and complex structures are presented to demonstrate the accuracy, stability and effect of wavefield simulation and RTM by the fourth order accuracy SBPFDM in boundary-conforming grids, and to exhibit the superiority of the fourth order method in efficiency and storage.

2. Methods

2.1. Acoustic wave equation and reverse time migration in boundary-conforming coordinates

The two-dimensional acoustic wave equation in second order formulation in Cartesian coordinate system (x,z) takes the form of

$$\frac{1}{v^2(x,z)}\frac{\partial^2 u}{\partial t^2} = \frac{\partial^2 u}{\partial x^2} + \frac{\partial^2 u}{\partial z^2}, \tag{1}$$

Fig. 1. Model 1 with a surface topography. A point source marked as an asterisk is located at (2000 m, 37 m).

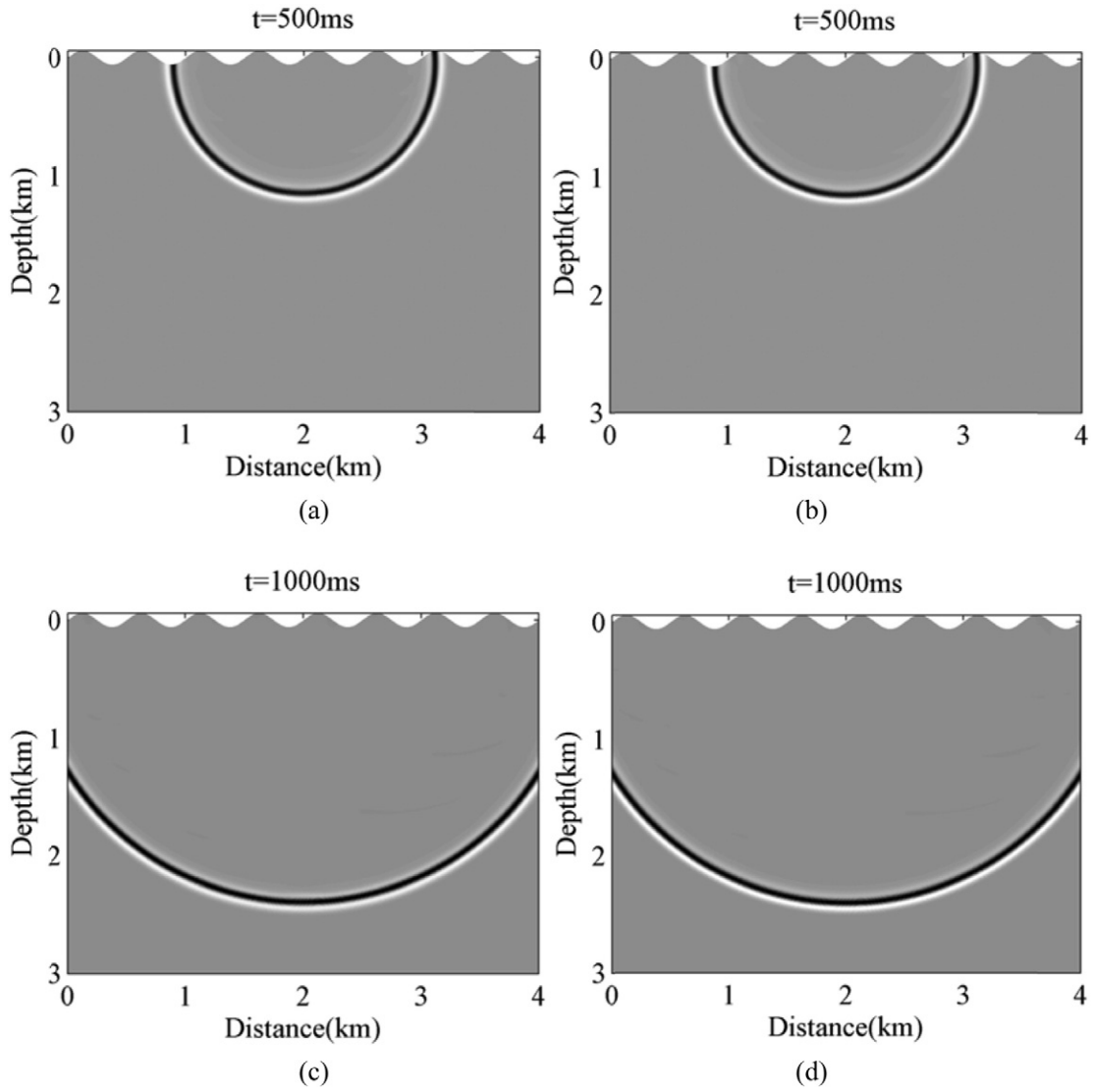where $v(x,z)$ is the velocity of the media, and $u(x,z)$ is the displacement.

Fig. 2. Snapshots at 500 ms (a) and (b), and 1000 ms (c) and (d) obtained by SBPFDM of second (a) and (c) and fourth order accuracy (b) and (d). The spatial interval is $\Delta q = \Delta r = 4.0$ m.
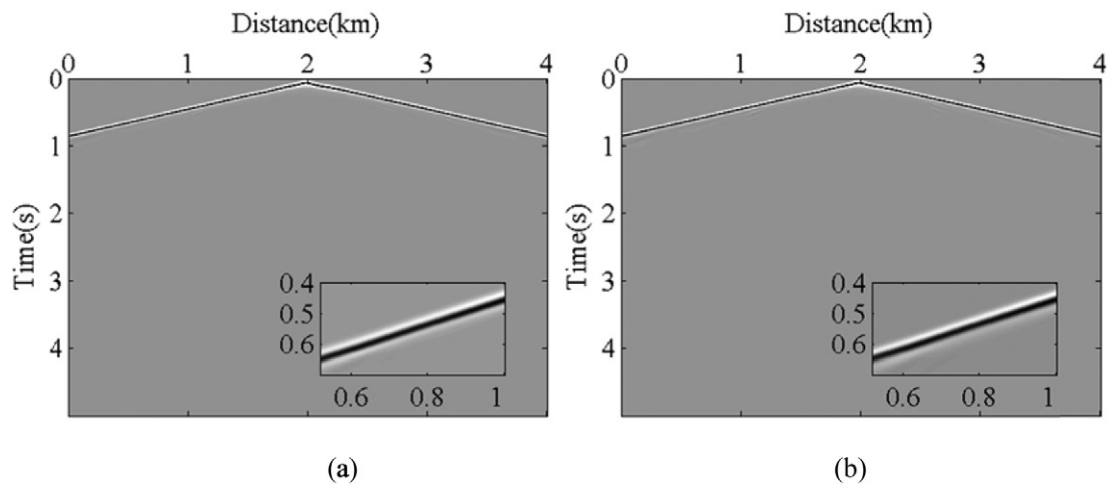

Fig. 3. Shot gathers of Model 1 computed by the SBPFDM of second (a) and fourth order accuracy (b). A part of zoomed direct wave is shown. The spatial interval is $\Delta q = \Delta r = 4.0$ m.
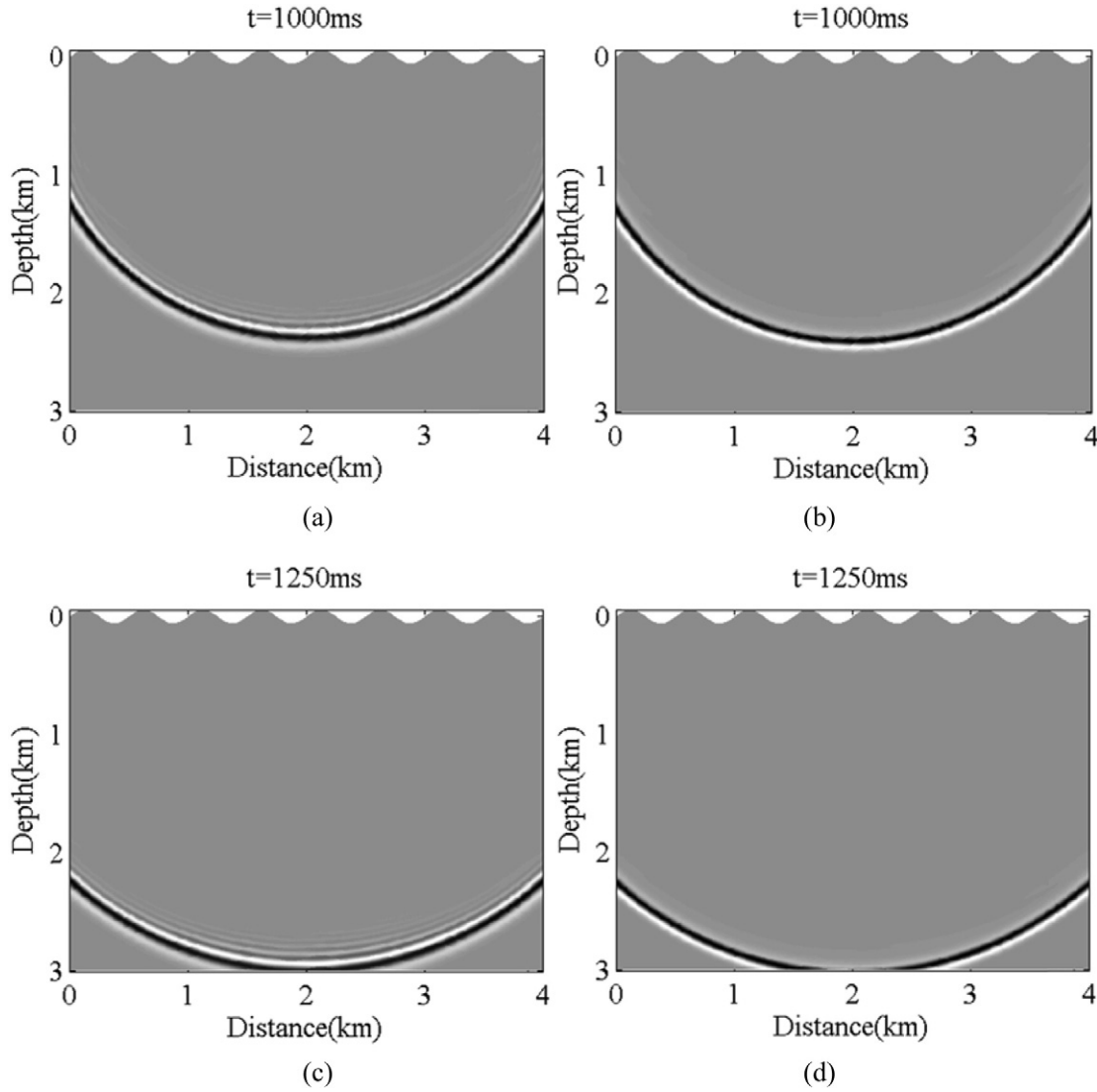
Fig. 4. Snapshots at 1000 ms (a) and (b), and 1250 ms (c) and (d) obtained by the SBPFDM of second (a) and (c) and fourth order accuracy (b) and (d). The spatial interval is $\Delta q = \Delta r = 8.0$ m.

In boundary-conforming coordinate system (q, r) generated by elliptic method (Thompson et al., 1977a, 1977b; Wei et al., 2000), Eq. (1) is reformulated as

$$\frac{J}{v^2}\frac{\partial^2 u}{\partial t^2} = \frac{\partial}{\partial q}\left(M_{qq}\frac{\partial u}{\partial q}\right) + \frac{\partial}{\partial q}\left(M_{qr}\frac{\partial u}{\partial r}\right) + \frac{\partial}{\partial r}\left(M_{qr}\frac{\partial u}{\partial q}\right) + \frac{\partial}{\partial r}\left(M_{rr}\frac{\partial u}{\partial r}\right), (2)$$

where $J = x_q z_r - x_r z_q$, $M_{qq} = J(q_x^2 + q_z^2)$, $M_{qr} = J(q_x r_x + q_z r_z)$, $M_{rr} = J(r_x^2 + r_z^2)$. x_q denotes $\partial x(q,r)/\partial q$, x_{qq} denotes $\partial^2 x(q,r)/\partial q^2$, and similarly in other cases. The structure of Eq. (2) is symmetric and compact, which favors efficient computation. However, Eq. (2) becomes more complicated with four additional coefficients. In special, when $J = 1$, $M_{qq} = 1$, $M_{qr} = 0$, $M_{rr} = 1$, Eq. (2) reduces to the form of acoustic wave Eq. (1) in Cartesian coordinate system. After the realization of coordinate transformation, one can easily conduct the acoustic wavefield simulation in irregular regions by solving Eq. (2).

RTM has been known as a powerful tool for imaging steeply dipping reflectors and complex structures in complicated velocity models. Using the boundary-conforming grids, RTM can be extended to irregular regions with arbitrary surface topography and interfaces. RTM in boundary-conforming coordinate system is similar to that in the Cartesian coordinate system, involving the source wavefield propagation along the positive time direction, the receiver wavefield propagation along the negative time direction, and the application of imaging conditions. Here, we choose the zero-lag cross-correlation imaging condition

$$I(q, r) = \int S(q, r, t)R(q, r, t)dt, \quad (3)$$

because it provides correct kinematics and is easy to implement. In Eq. (3) $I(q, r)$ stands for the imaging function, $S(q, r, t)$ and $R(q, r, t)$ represent the source and receiver extrapolated wavefield respectively.

2.2. Perfectly matched layer in boundary-conforming coordinates

The PML technique is used for truncating unbounded domains. Originally proposed by Berenger (1994) and later improved by many others, PML has been very successful for electromagnetic wave simulations. PML has superior non-reflecting properties (Chen et al., 2013). It is
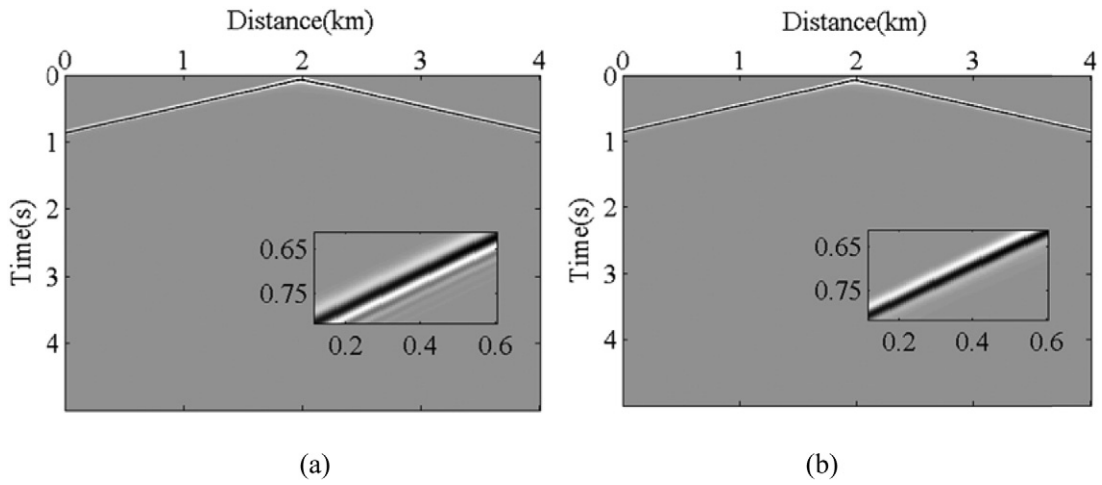
Fig. 5. Shot gathers of Model 1 obtained by the SBPFDM of second (a) and fourth order accuracy (b). The spatial interval is Δq = Δr = 8.0 m.
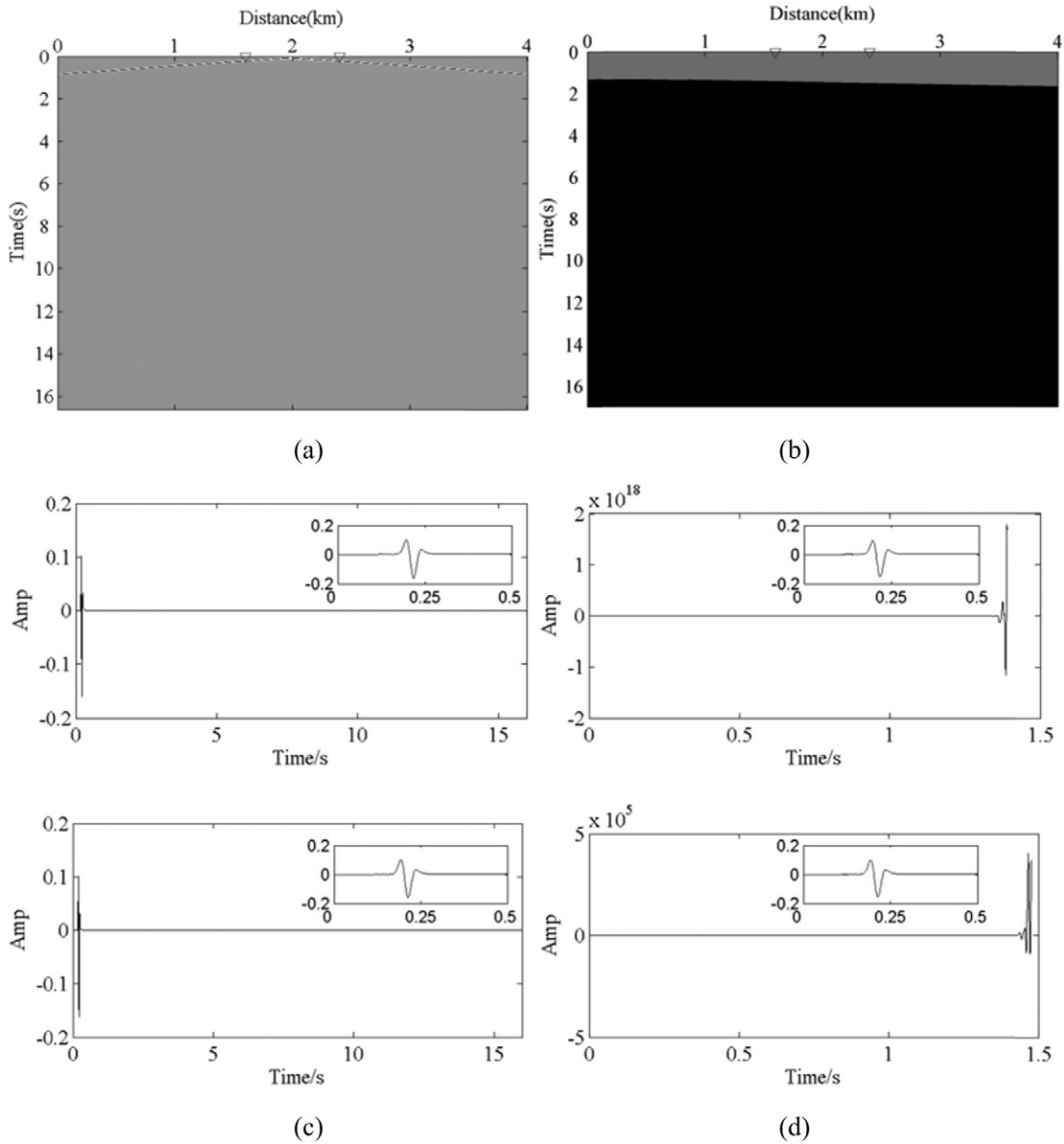

Fig. 6. Shot gathers (a) and (b) of Model 1 and corresponding seismograms of two receivers (c) and (d) obtained by the SBPFDM with temporal intervals of 0.83 ms (a), (c) and 0.85 ms.
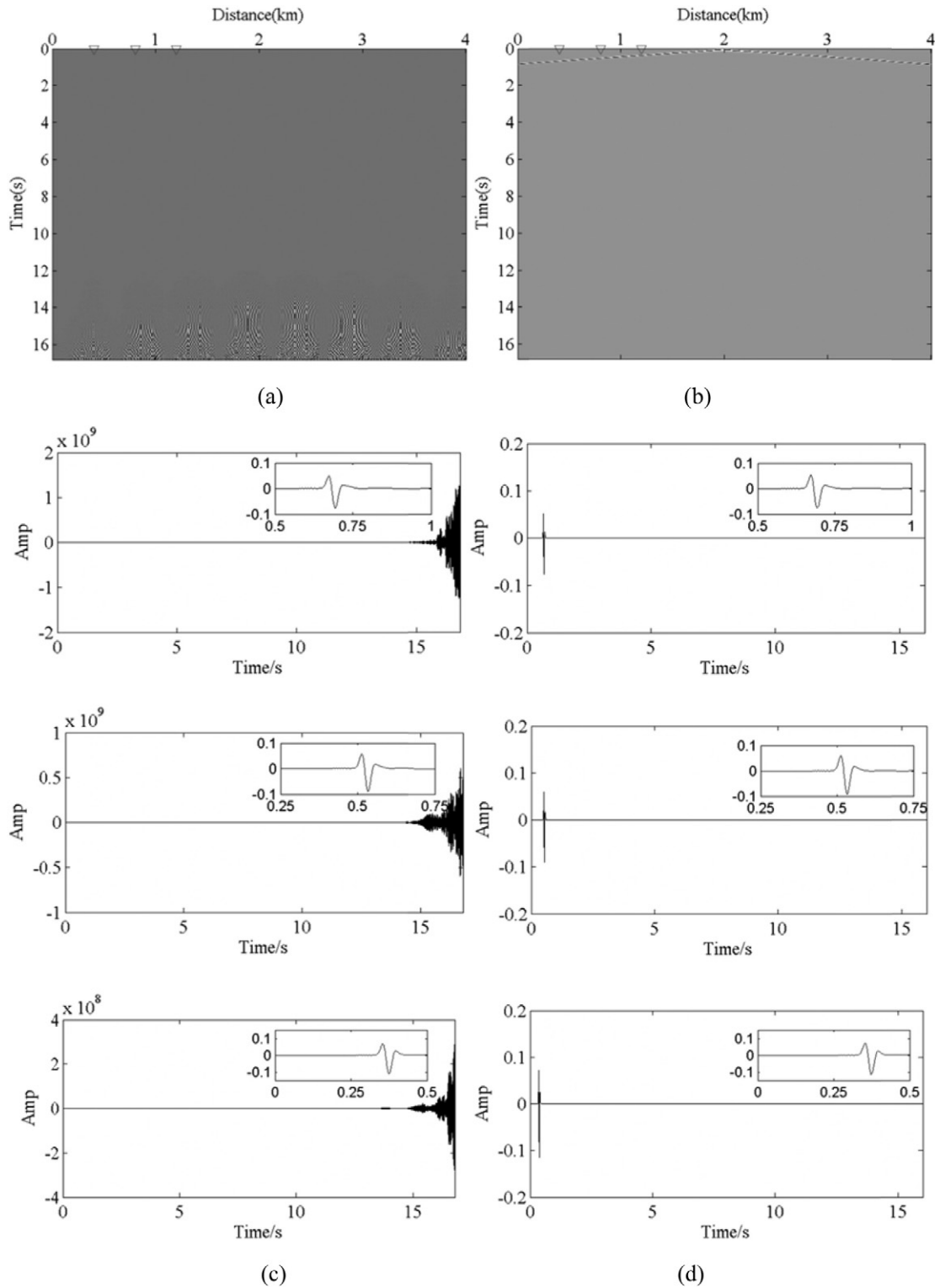
Fig. 7. Shot gathers (a) and (b) of Model 1 and corresponding seismograms of two receivers (c) and (d) obtained by the central FDM (a), (c) and SBPFDM (b), (d). The temporal interval is $\Delta t = 0.84$ ms. The locations of receivers are marked by inverted triangles in (a) and (b).

pointed out that the PML technique has stability issues when applied to the elastic wave equation and some anisotropic wave equations, where heterogeneous material properties and free surface boundary conditions can cause instability (Petersson and Sjögreen, 2009, 2014; Sjögreen and Petersson, 2014). It makes the super-grid technique an alternative for elastic wave equation in curvilinear grids. However, the

super-grid technique cannot achieve the "perfect" non-reflecting property of PML (Petersson and Sjögreen, 2015). Since our method is based on the acoustic wave equation in second order displacement formulation, the instability encountered in elastic wave equation can be avoided. With a lot of evidence to show the effect of PML in boundary-conforming grids for acoustic wave equation (e.g. Rao and
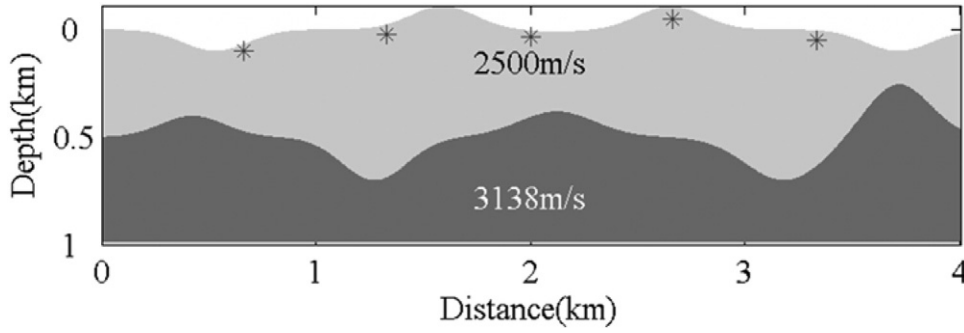
Fig. 8. Model 2 with surface topography and an irregular interface. Point sources marked as asterisks are located at (664 m,93 m), (1328 m,15 m), (2000 m,29 m), (2664 m,−59 m), (3328 m,44 m).

Wang, 2013; Yuan et al., 2014; Wang et al., 2015), or elastic wave equation (e.g. Lan et al., 2016), the PML technique is applied to suppress the artificial reflections in this paper.

Considering attenuations along the q- and r-axis simultaneously, the scalar u is split into three terms, $u = u_1 + u_2 + u_3$, u_1, u_2, u_3 represent the splitting displacements. The time domain split PML formulae with a symmetric and compact form in boundary-conforming coordinate system are expressed as

$$
\begin{cases}
\dfrac{J}{v^2}(\partial_t + d_q)^2 u_1 = \dfrac{\partial}{\partial q}\left(M_{qq}\dfrac{\partial u}{\partial q}\right) - M_{qq}\dfrac{\partial d_q}{\partial q}\exp(-d_q t) * \dfrac{\partial u}{\partial q}, \\
\dfrac{J}{v^2}(\partial_t + d_q)(\partial_t + d_r)u_2 = \dfrac{\partial}{\partial q}\left(M_{qr}\dfrac{\partial u}{\partial r}\right) + \dfrac{\partial}{\partial r}\left(M_{qr}\dfrac{\partial u}{\partial q}\right), \\
\dfrac{J}{v^2}(\partial_t + d_r)^2 u_3 = \dfrac{\partial}{\partial r}\left(M_{rr}\dfrac{\partial u}{\partial r}\right) - M_{rr}\dfrac{\partial d_r}{\partial r}\exp(-d_r t) * \dfrac{\partial u}{\partial r},
\end{cases}
\tag{4}
$$

where d_q and d_r represent the damping functions in the PML region, and $*$ stands for temporal convolution. Eq. (4) is applied to the PML regions to attenuate the wavefield exponentially, and the original wave Eq. (2) is solved in the interior regions.

2.3. Discretization and stability analysis

The major innovation of this paper lies in the application of the fourth order SBP finite difference scheme to acoustic wavefield simulation and RTM in boundary- conforming grids. The key ingredient of SBP method is the discretization of second derivative with variable coefficient, which satisfies a summation by parts identity and guarantees stability of the scheme. The discretization is consistent with previous summation by parts stencils for approximating first derivatives (e.g. Strand, 1994; Carpenter et al., 1999; Mattsson, 2003; Sjögreen and Petersson, 2012). Higher order summation by parts operators for approximating first derivatives are well known (for example, Strand, 1994). Operators in the literature approximate the first derivative to pth order accuracy in the interior, for $p = 2,4,6,8,10$. We mainly focus on the case of $p = 4$ in the component form in this paper. Similar as the fourth order accuracy FDM in Cartesian coordinate system, the fourth order accuracy SBPFDM in boundary-conforming grids is advantageous in suppressing the numerical dispersion and improving the efficiency. Here, the SBP finite difference scheme is adopted on non-staggered grids for discretizing Eqs. (2) and (4). We discretize the medium with the nodes

$$q_i = (i-1)\Delta q, \quad i = 1, \dots, N_q,$$

$$r_j = (j-1)\Delta r, \quad j = 1, \dots, N_r,$$

where Δq and Δr are the intervals in the q- and r-directions, i,j are the indexes of spatial steps, N_q and N_r are the number of grid nodes in q- and r- directions respectively.

With the introduction of the operator D and G to denote the fourth order accuracy SBP finite difference approximations of the first and second derivative in the interior (r-direction for example)

$$
D^{(r)}u_j = \frac{1}{12\Delta r}\left(-u_{j+2} + 8u_{j+1} - 8u_{j-1} + u_{j-2}\right) = u_r(r_j) + O\left(h^4\right), \tag{5}
$$

$$
\begin{aligned}
G^{(r)}(\sigma)u_j &= \frac{1}{12\Delta r^2}\left(\begin{array}{l}E^r(\sigma_{j-1})(u_j - u_{j-2}) - 16E^r(\sigma_{j-1/2})(u_j - u_{j-1}) \\ +16E^r(\sigma_{j+1/2})(u_{j+1} - u_j) - E^r(\sigma_{j+1})(u_{j+2} - u_j)\end{array}\right), \\
&= \frac{\partial}{\partial r}\left(\sigma\frac{\partial u}{\partial r}\right) + O\left(h^4\right)
\end{aligned}
\tag{6}
$$

and the averaging operators

$$
E^r(\sigma_j) = \frac{1}{2}\left(3\sigma_{j-1} - 4\sigma_j + 3\sigma_{j+1}\right), \tag{7}
$$

$$
E^r(\sigma_{j+1/2}) = \frac{1}{8}\left(\sigma_{j-1} + 3\sigma_j + 3\sigma_{j+1} + \sigma_{j+2}\right), \tag{8}
$$

Eq. (2) is discretized as

$$
\frac{J}{v^2}\frac{u^{k+1} - 2u^k + u^{k-1}}{\Delta t^2} = \begin{array}{l}G^{(q)}(M_{qq})u^k + D^{(q)}\left(M_{qr}D^{(r)}u^k\right) \\ +D^{(r)}\left(M_{qr}D^{(q)}u^k\right) + G^{(r)}(M_{rr})u^k\end{array}, \tag{9}
$$

where Δt is the time interval, and k is the index of time step.

Similarly, the application of finite difference operators to Eq. (4) leads to

$$
\begin{cases}
u_1^{k+1} = \dfrac{1}{1 + d_q\Delta t}\left\{\begin{array}{l}\left(2 - d_q^2\Delta t^2\right)u_1^k - (1 - d_q\Delta t)u_1^{k-1} \\ + \dfrac{v^2\Delta t^2}{J}\left[G^{(q)}(M_{qq})u^k + M_{qq}C_1^k\right]\end{array}\right\}, \\[4mm]
u_2^{k+1} = \dfrac{1}{1 + \dfrac{d_q + d_r}{2}\Delta t}\left\{\begin{array}{l}(2 - d_q d_r\Delta t^2)u_2^k - \left(1 - \dfrac{d_q + d_r}{2}\Delta t\right)u_2^{k-1} \\ + \dfrac{v^2\Delta t^2}{J}\left[D^{(q)}\left(M_{qr}D^{(r)}u^k\right) + D^{(r)}\left(M_{qr}D^{(q)}u^k\right)\right]\end{array}\right\}, \\[4mm]
u_3^{k+1} = \dfrac{1}{1 + d_r\Delta t}\left\{\begin{array}{l}\left(2 - d_r^2\Delta t^2\right)u_3^k - (1 - d_r\Delta t)u_3^{k-1} \\ + \dfrac{v^2\Delta t^2}{J}\left[G^{(r)}(M_{rr})u^k + M_{rr}C_2^k\right]\end{array}\right\},
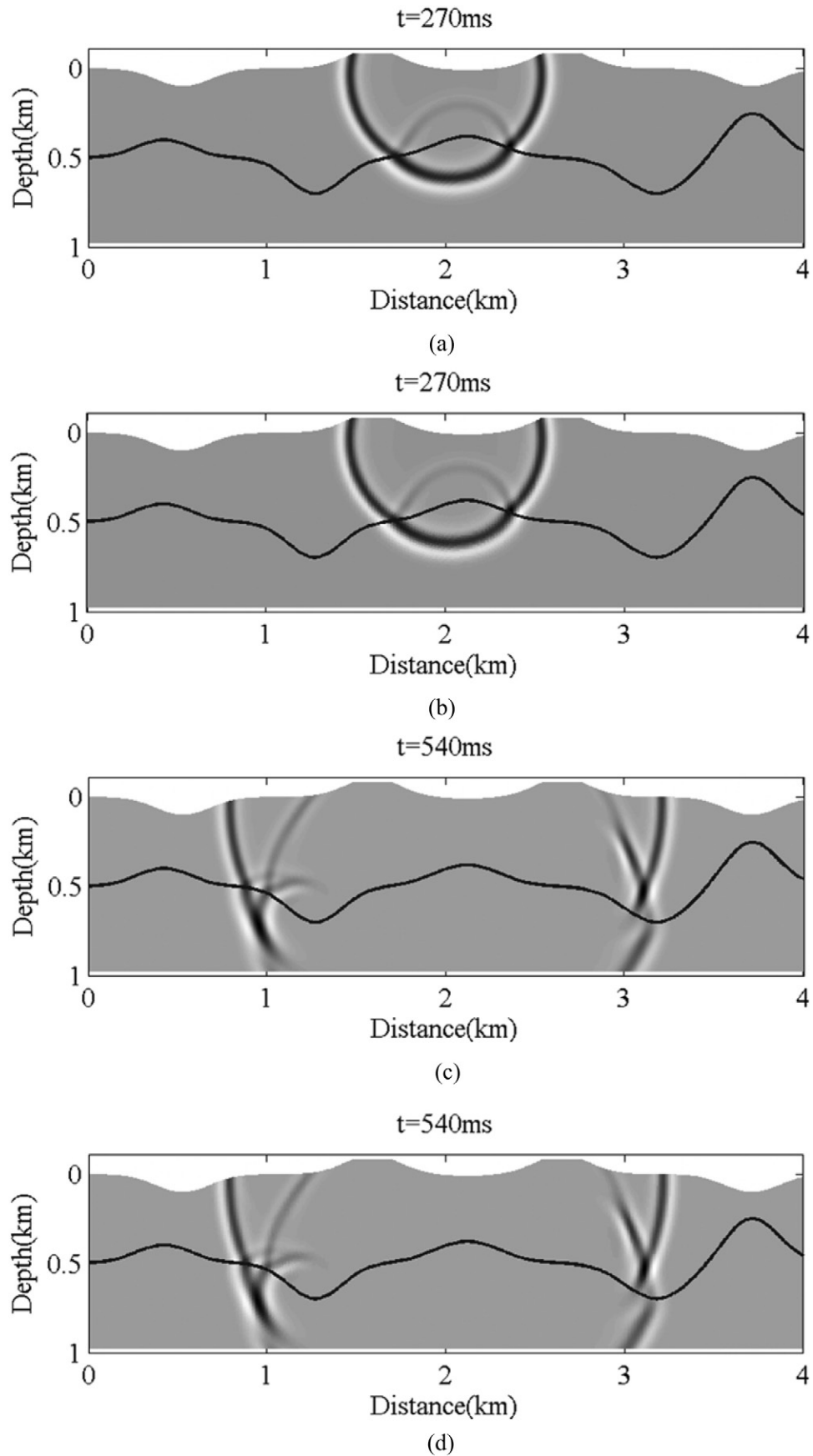\end{cases}
\tag{10}
$$

Fig. 9. Snapshots of Model 2 computed by the second (a) and (c) and fourth (b) and (d) order SBPFDM. (a) and (b) at 270 ms, (c) and (d) at 540 ms.
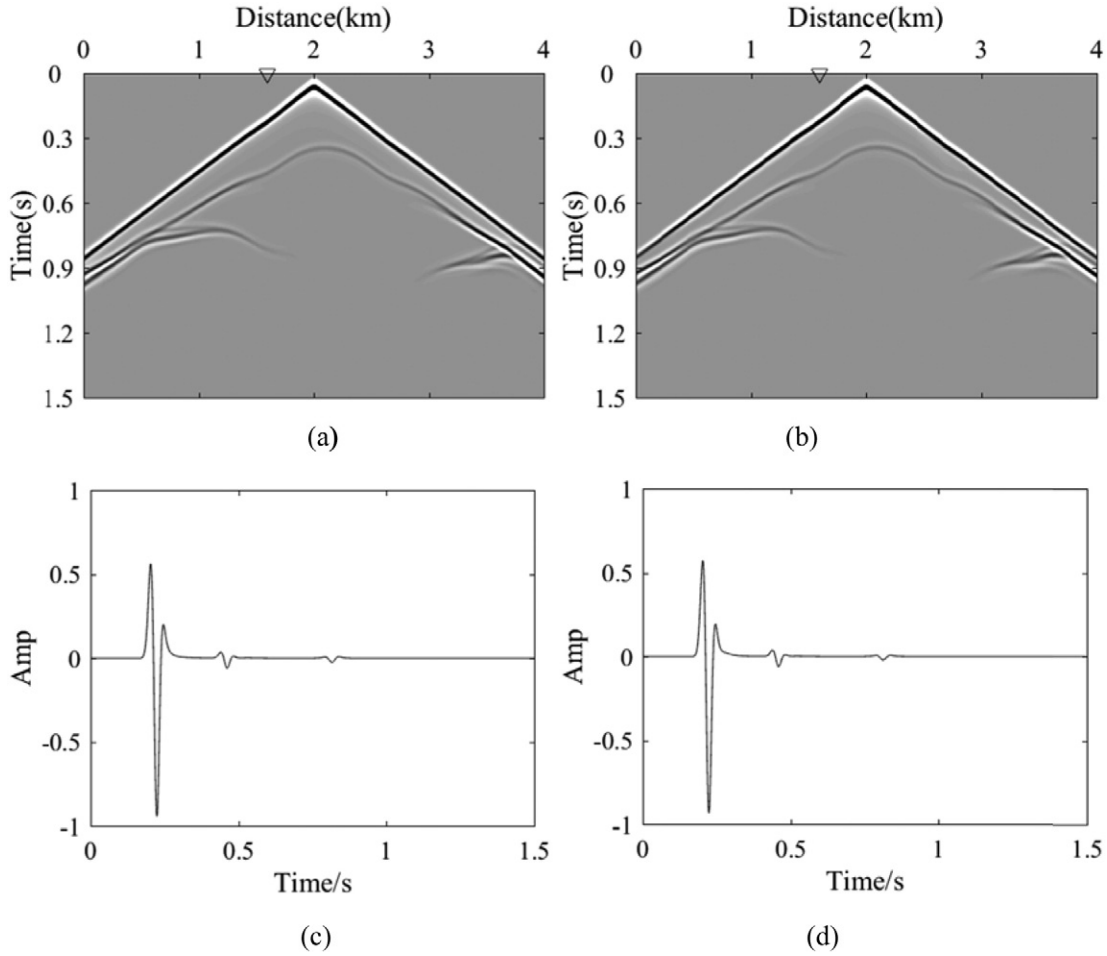
Fig. 10. Shot gathers (a) and (b) of Model 2 and corresponding seismograms of one receiver (c) and (d) calculated by the second (a), (c) and fourth (b), (d) order SBPFDM. The locations of receivers are marked by inverted triangles in (a) and (b).

where

$$C_1^k = -\frac{\partial d_q}{\partial q} \exp(-d_q t) * \left.\frac{\partial u}{\partial q}\right|^k$$
$$= \exp(-d_q \Delta t) C_1^{k-1} - \frac{\Delta t}{2}\frac{\partial d_q}{\partial q}\left[\exp(-d_q \Delta t)D^{(q)}u^{k-1} + D^{(q)}u^k\right],$$

and

$$C_2^k = -\frac{\partial d_r}{\partial r} \exp(-d_r t) * \left.\frac{\partial u}{\partial r}\right|^k$$
$$= \exp(-d_r \Delta t) C_2^{k-1} - \frac{\Delta t}{2}\frac{\partial d_r}{\partial r}\left[\exp(-d_r \Delta t)D^{(r)}u^{k-1} + D^{(r)}u^k\right].$$

The variables of $u_i(i = 1, 2, 3)$ in Eq. (10) are computed respectively to constitute $u = \sum_{i=1}^{3} u_i$, which represents the wavefield in the PML region.

Eq. (9) is stable under the time step restriction of

$$\Delta t \leq \frac{\sqrt{3}/2}{v\sqrt{\frac{1}{J}\left(\frac{M_{qq}}{h_q^2} + \frac{M_{rr}}{h_r^2}\right)}} \tag{11}$$

The derivation of Eq. (11) is given in Appendix A. The application of SBP operator in boundary-conforming grids leads to an attractive stability advantage over traditional central finite difference scheme.

3. Numerical examples

Three simulation examples (Model 1, 2 and 3) are presented to evaluate the performances of the fourth order accuracy SBP finite difference scheme for wavefield simulation and RTM in boundary-conforming grids via elliptic method. The PML absorbing boundary condition (4) is enforced to suppress the artificial reflections. Thirty-layer PMLs are applied to each side of the models. Simulations by the SBP finite difference scheme of second and fourth order accuracy are individually performed to compare the accuracy and efficiency. Simulation results by fourth order SBP scheme with different temporal intervals are compared to verify the correctness of the stability condition (11). Comparisons between the simulations by fourth order accuracy SBP and central finite difference schemes are also respectively conducted to illustrate the stability advantage of SBP operator. The positive r-axis is assumed downward in numerical models. All numerical examples are performed on a personal computer equipped by CPU of Intel Core i7, 2.4GHz.

3.1. Sinusoidal surface homogeneous model

Model 1 with sinusoidal surface topography is designed with two purposes: firstly, to compare the simulations in complicated domains by the SBPFDM of second and fourth order, and secondly, to verify the stability condition (11) and to illustrate the stability advantage of SBPFDM over the central FDM. For simplicity, the velocity is a constant illustrated in Fig. 1. The size of the model is 4000 m × 3000 m. One point source of Ricker wavelet with the dominant frequency of 20 Hz
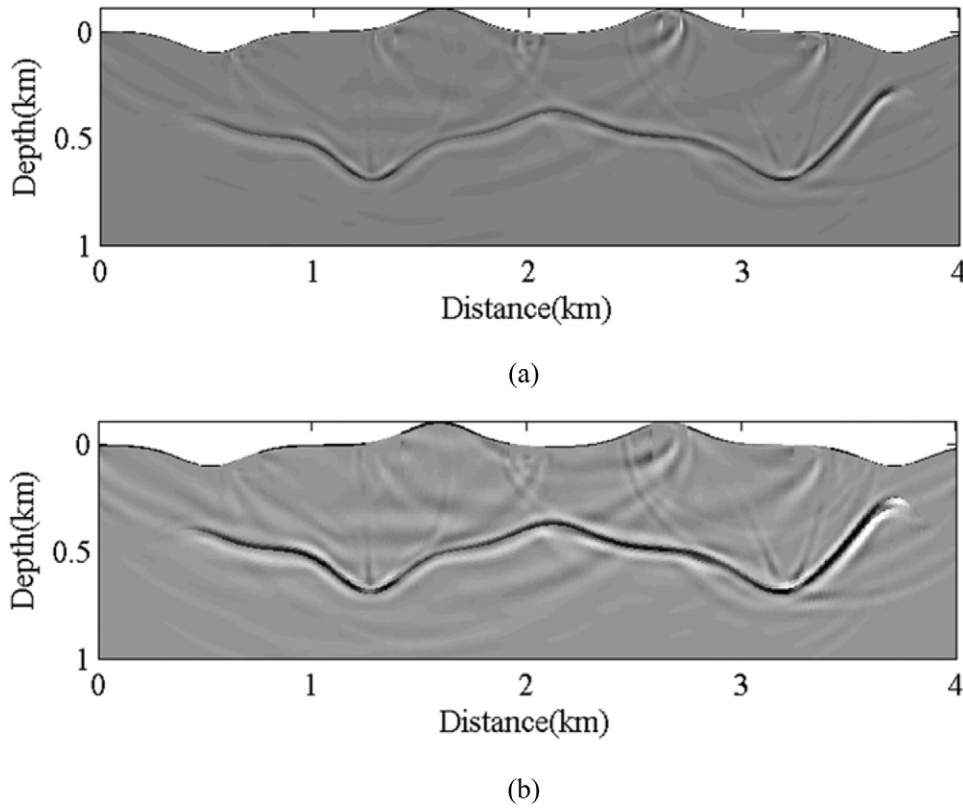
(a)

(b)

Fig. 11. RTM results of Model 2 obtained by the second (a) and fourth (b) order SBPFDM.

is located at (2000 m, 37 m), which is marked as an asterisk in Fig. 1. The receivers are placed along the surface.

(1) Comparisons between the SBPFDM of second and fourth order.

Two groups of parameters, including the spatial interval, temporal interval and size of grids, are set for simulation as follows. Group 1: $\Delta q = \Delta r = 4.0$ m, $\Delta t = 0.5$ ms, $N_q = 1001$, $N_r = 751$; Group 2: $\Delta q = \Delta r = 8.0$ m, $\Delta t = 0.5$ ms, $N_q = 501$, $N_r = 376$. Each group of parameters is applied to both simulations by the second and fourth order accuracy finite difference schemes.

Figs. 2 and 3 illustrate the simulation results by the parameters in Group 1. Fig. 2(a)–(d) depicts snapshots of wavefield at 500 ms and 1000 ms respectively, where Fig. 2(a) and (c) are simulated by the second order SBPFDM, and Fig. 2(b) and (d) are those of the fourth order SBPFDM. Shot gathers obtained by the two accuracy SBPFDMs are shown in Fig. 3. For seeing clearly the simulation results, zoomed part of the direct wave is shown in the lower right corner of Fig. 3(a) and (b). Since the spatial interval is fine, the two simulation results are similar. The effect of PMLs is also validated in the simulations.

Figs. 4 and 5 illustrate the simulation results by the parameters in Group 2. Fig. 4(a)–(d) depicts snapshots of wavefield at 1000 ms and 1250 ms respectively, where Fig. 4(a) and (c) are simulated via the second order SBPFDM, and Fig. 4(b) and (d) are by the fourth order SBPFDM. The simulation result obtained by the fourth order method is accurate, however, that by the second order scheme suffers from the numerical dispersion. Shot gathers calculated by these two schemes are shown in Fig. 5. The simulation results calculated by the second

order accuracy method (Fig. 5a) show evident numerical dispersion, while those obtained by using the fourth order accuracy method are free of dispersion (Fig. 5b).

The simulation results obtained by using different accuracy methods with different spatial intervals show that the fourth order accuracy SBPFDM is more advantageous in suppressing numerical dispersion. To achieve a desired accuracy, the use of the fourth order accuracy SBPFDM reduces the number of points needed in the discretization and consequently reduces the computational cost.

(2) Comparisons between fourth order accuracy SBPFDM and central FDM.

Simulation results via fourth order SBP scheme with different temporal intervals are compared to verify the correctness of the stability condition (11). According to (11), the time step restriction that ensures the stability of fourth order accuracy SBPFDM in boundary-conforming grids for Model 1 is $\Delta t \leq 0.84$ ms. Two temporal intervals, $\Delta t = 0.83$ ms and $\Delta t = 0.85$ ms, are used for simulations respectively. Stable simulation as illustrated in Fig. 6 (a) and (c) is obtained by using $\Delta t = 0.83$ ms. However, the simulations by using $\Delta t = 0.85$ ms suffer from instability, i.e., overflow occurs during simulation. The wavelet is covered up by the overflow (Fig. 6d), resulting in error information in the shot gathers (Fig. 6b).

The locations of receivers are marked by inverted triangles in (a) and (b).

The simulations by central finite difference and SBP methods are compared to illustrate the stability superiority of SBP operator in boundary-

Table 1
Elapse time and storage requirement of RTM per shot for Model 2 tested with the second and fourth order SBPFDM.

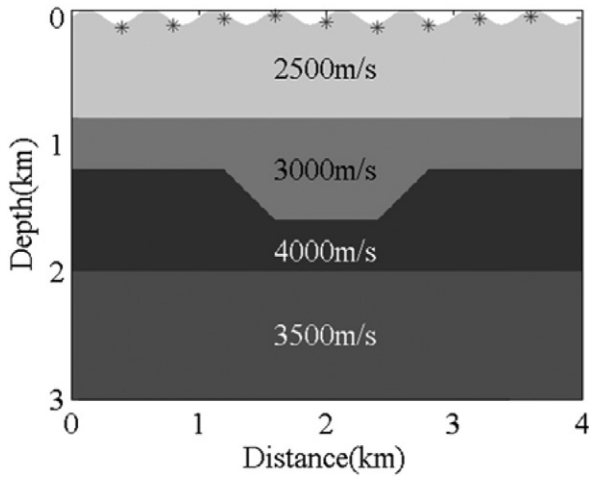| Accuracy	Grid size	The number of grids	Time step	Temporal sampling points	Elapse time	Storage requirement
2nd order	4 m	1001×251	0.3 ms	10,000	289.8 s	12.2 GB
4th order	8 m	501×126	0.6 ms	5000	83.3 s	1.94 GB
Savings		75%		50%	71.26%	84.10%

Fig. 12. Model 3 with sinusoidal topography and a depression, 9 sources are marked as asterisks.

conforming grids. The accuracy is fourth order and the spatial interval is $\Delta q = \Delta r = 4.0$ m for both methods. The critical value of $\Delta t = 0.84$ ms from the stability condition (11) is used as the temporal interval in the

simulations. The results by central finite difference method are not stable, as illustrated in Fig. 7(a) and (c). The application of SBP finite difference method guarantees the stability of the simulations (Fig. 7b, d). These simulations prove the stability superiority of SBPFDM over central finite difference scheme in boundary-conforming grids.

3.2. Two-layer model with irregular surface and interface

Model 2 with surface topography and an irregular interface is designed to test the effect and efficiency of RTM performed by the fourth order SBPFDM in complicated domains. The surface undulation represents topography with a combination of two hills and two depressions, as illustrated in Fig. 8, in which the velocities are given. The size of the model is 4000 m × 1000 m. Five point sources of Ricker wavelet with the dominant frequency of 20 Hz are located at (664 m, 93 m), (1328 m, 15 m), (2000 m, 29 m), (2664 m, −59 m), (3328 m, 44 m) marked as asterisks. The receivers are placed along the surface at all grids.

To compare the efficiency, both the second and fourth order SBPFDM are applied for the simulation and RTM. Given the fact that the second order method is more subject to grid dispersion, the spatial and temporal intervals for the second order method are $\Delta q = \Delta r = 4.0$ m and $\Delta t = 0.3$ ms, and those for the four order method are $\Delta q = \Delta r = 8.0$ m and $\Delta t = 0.6$ ms.
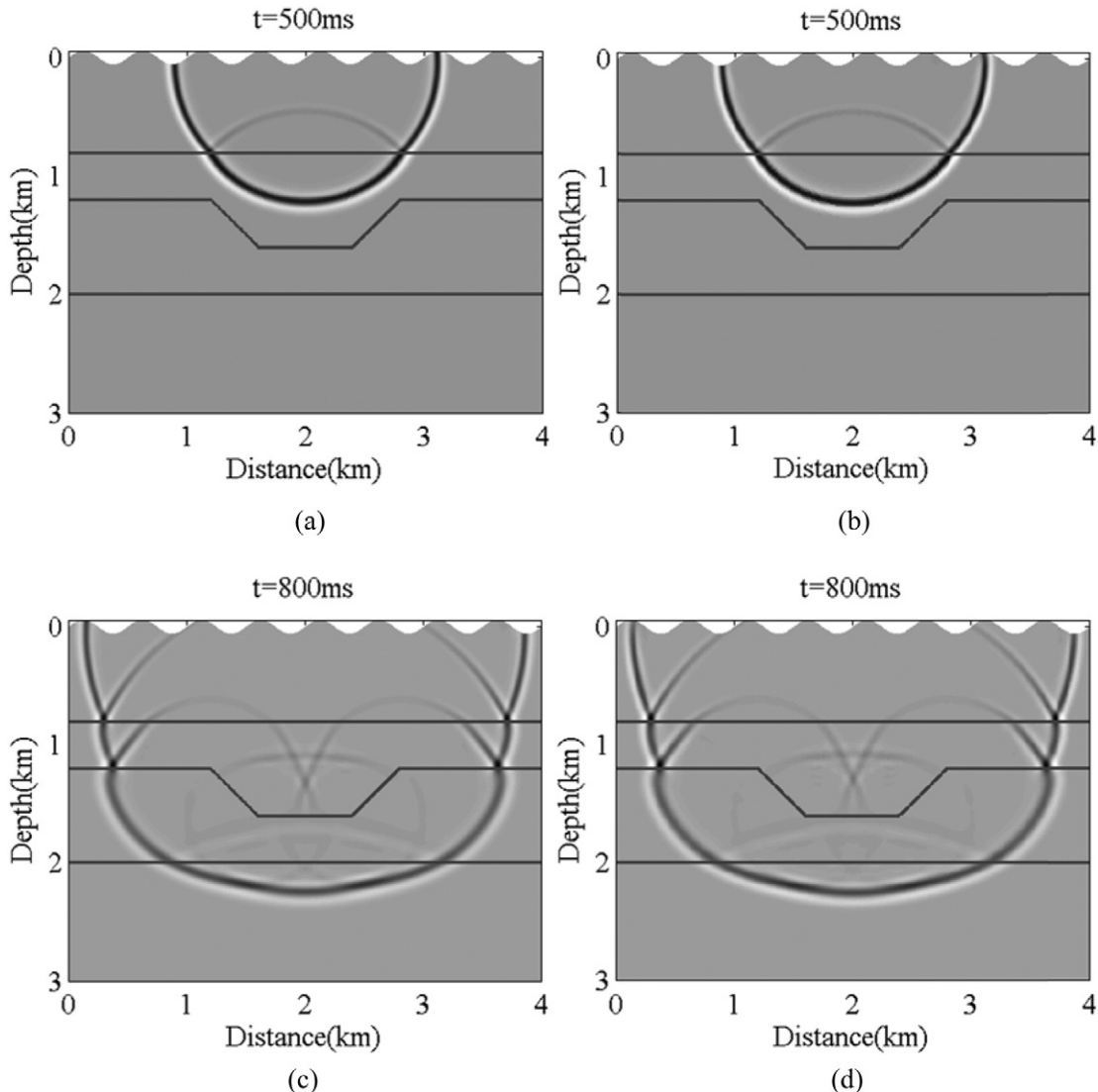

(a)

(b)

(c)

(d)

Fig. 13. Snapshots for Model 3 calculated by the second (a) and (c) and fourth (b) and (d) order SBPFDM. (a) and (b) at 500 ms, (c) and (d) at 800 ms.
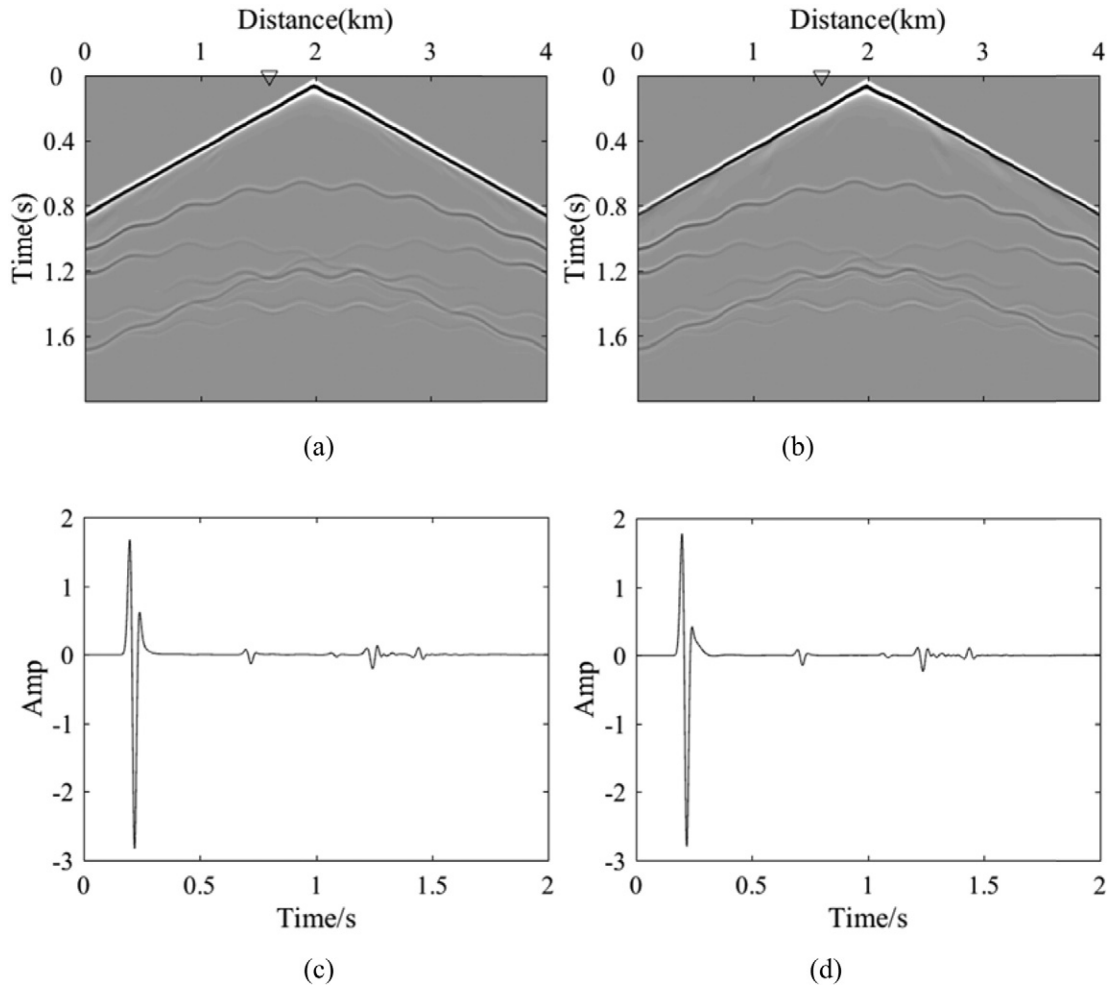
Fig. 14. Shot gathers (a) and (b) of Model 3 and corresponding seismograms of one receiver (c) and (d) computed by the SBPFDM of (a), (c) second and (b), (d) fourth order accuracy. The locations of receivers are marked by inverted triangles in (a) and (b).

Fig. 9 depicts snapshots of wavefield at 270 ms and 540 ms calculated by the second and fourth order accuracy methods, excited at (2000 m, 29 m). The black lines in the snapshots indicate the interface. It is seen from Fig. 9 that the wavefields are correctly simulated by the two methods, with reflections arising at the interface and no artificial reflection occurring near the boundary. Shot gathers and corresponding seismograms of one receiver obtained by the two methods are similar as shown in Fig. 10, where the locations of receivers are marked by

inverted triangles. The direct wave and reflections are clear in the shot gathers. Due to the surface topography, the travel time curve for the direct wave is not a straight line. Fig. 11 gives the RTM results obtained by the second and fourth order accuracy SBPFDM. The migration results are basically consistent with the interface for both methods. It should be noted that the images have been filtered by a Laplacian filter (Zhang and Sun, 2009) to suppress low frequency artifacts. The artifacts will become weak if the number of sources increases.
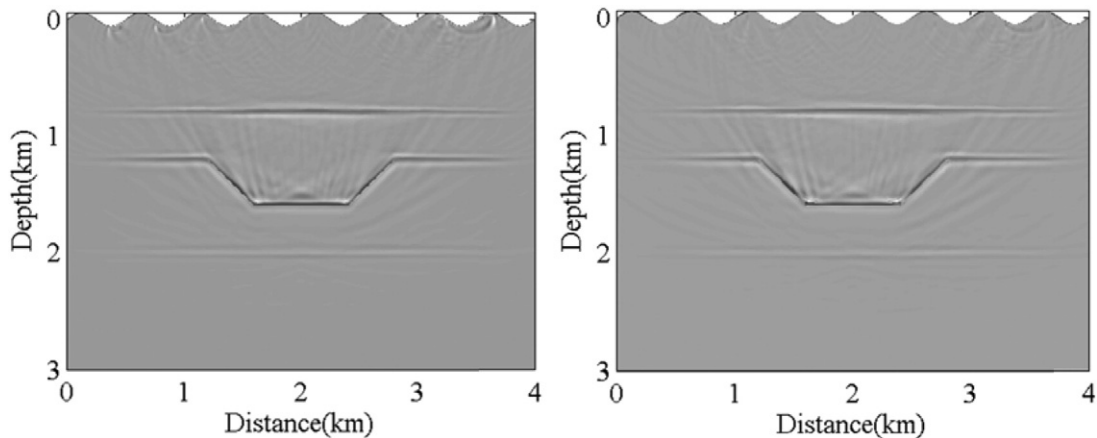

Fig. 15. RTM results of Model 3 calculated by the SBPFDM of (a) second and (b) fourth order accuracy.

Table 2
Elapse time and storage requirement of RTM per shot for Model 3 tested with the second and fourth order SBPFDM.

Accuracy	Grid size	The number of grids	Time step	Temporal sampling points	Elapse time	Storage requirement
2nd order	4 m	1001×751	0.2 ms	10,000	986.2 s	32.055 GB
4th order	8 m	501×376	0.4 ms	5000	180.0 s	4.556 GB
Savings		75%		50%	81.75%	85.79%

Although the effects of snapshots, shot gathers and migration results are similar for the second and fourth accuracy SBPFDM, the elapse CPU time and storage requirement are quite different. The details of the costs for RTM per shot for Model 2 by the two methods are listed in Table 1. The low dispersion allows the fourth order SBPFDM to use a coarser grid, which is 2 times of the grid in the second order method, thus the number of grids for the fourth order method is 75% less than that for the second order method. According to the stability condition, a coarser grid indicates that a larger time interval (2 times of that in the second order method) can be used. For a given length of record, the temporal sampling points in the fourth order method are only half of those in the second order method. When applying the fourth order method, it takes only 28.74% of the elapse time and 15.9% of the storage of the second order method. The efficiency is greatly improved and the storage is significantly decreased by the fourth order accuracy SBPFDM, with the comparable simulation and migration results.

3.3. Multi-layer model with sinusoidal topography and a depression

Model 3 shown in Fig. 12 having a sinusoidal topography and a depression is built to further verify the applicability and efficiency of wavefield simulation and RTM by the fourth order accuracy SBPFDM in irregular domains by boundary-conforming grids. The size of the model is 4000 m × 3000 m. Nine point sources marked as asterisks are located at (400 m, 84 m), (800 m, 67 m), (1200 m, 8 m), (1600 m, − 9 m), (2000 m, 38 m), (2400 m, 85 m), (2800 m, 67 m), (3200 m, 9 m), (3600 m, − 9 m). The receivers with a spatial interval of Δq are placed along the surface. The record length is 2 s. Similar to Model 2 case, both the second and fourth order accuracy SBPFDM are applied to the simulations and RTM. For the second order method, $\Delta q = \Delta r = 4.0$ m and $\Delta t = 0.2$ ms, and for the fourth order one, $\Delta q = \Delta r = 8.0$ m and $\Delta t = 0.4$ ms.

Fig. 13 exhibits the wavefield snapshots at 500 ms and 800 ms obtained by the second and fourth order accuracy SBPFDM, in which the interfaces are indicated. Because of the existence of two planar interfaces and a depression, the wavefield is complicated with plentiful reflections. It is obvious that the simulation results for these two methods are similar.

Shot gathers and corresponding seismograms of one receiver calculated by these two methods are shown in Fig. 14. Direct wave and reflections are correctly and clearly presented in both the shot gathers, and no visible artificial reflections occur due to the application of PMLs. The shot gathers and the seismograms obtained by the methods with different accuracy are similar. Fig. 15 illustrates the RTM images obtained by the two methods. Similar to Model 2, the interfaces and the structure are well imaged. It means that either method is applicable to RTM by boundary-conforming grids in regions containing surface topography, complicated structure and irregular interface. The migration results by these two methods are similar.

Table 2 gives the costs of RTM per shot for Model 3 by these two methods. Similar to the cost analysis in Model 2, compared with the second order method, the application of coarser grid and larger time interval in the fourth order method decreases the numbers of grids and temporal sampling points to 25% and 50% respectively. In contrast to the second order method, the fourth order one can save 81.75% of CPU time and 85.79% of storage space. It can also be concluded that due to

the larger size of Model 3 than Model 2, the savings of CPU time and storage for RTM in Model 3 are more evident.

4. Conclusions

In this paper, we consider the extension of the second order SBPFDM for RTM and PMLs in boundary-conforming grids. The acoustic wave equation is reformulated to boundary-conforming coordinate system for wavefield simulation and RTM, and the corresponding PML formula is expressed symmetrically and compactly in such coordinate system. The fourth order SBPFDM is presented to discretize the wave equation and PML formulae. By comparing the simulation results of the second and fourth order SBPFDM, we illustrate the advantages of the fourth order one in high accuracy and low dispersion, allowing coarser grids. In addition, comparisons are conducted between the fourth order SBPFDM and central finite difference method, to illustrate the stability superiority of SBP operator. The results of RTM by both methods are proved satisfying with the structures and interfaces well imaged. However the fourth order accuracy scheme is shown to be substantially more efficient than the second order one, in both efficiency and memory requirement. Although the work in this paper is confined to two-dimensional regions, the ideas and equations can be easily extended to three dimensions, and it is our future work.

Appendix A. Stability analysis of Eq. (9)

In numerical computations, Fourier analysis is applied to analyze the stability of Eq. (9). Since Fourier analysis is limited to the periodic problem with homogeneous material properties, the parameters of M_{qq}, M_{rr} and J are assumed as constants. In boundary-conforming grids, $\beta = 0$ is essential to guarantee the orthogonality of the coordinate lines, it can be concluded that $M_{qr} = 0$. Thus Eq. (9) is simplified as

$$u^{n+1} - 2u^n + u^{n-1} = \frac{v^2 \Delta t^2}{J} \left[M_{qq} G^q(u^n) + M_{rr} G^r(u^n) \right]. \tag{A1}$$

The spatial finite difference operators in Eq. (A1) correspond to

$$
\begin{aligned}
G^q(u^n) &\to \frac{-e^{2ik_q h_q} + 16e^{ik_q h_q} - 30 + 16e^{-ik_q h_q} - e^{-2ik_q h_q}}{12h_q^2} \hat{u}^n \\
&= \frac{-4\sin^2 \frac{k_q h_q}{2} \left(\sin^2 \frac{k_q h_q}{2} + 3 \right)}{3h_q^2} \hat{u}^n \\
&:= \frac{-\psi(k_q)}{h_q^2} \hat{u}^n,
\end{aligned}
\tag{A2}
$$

$$G^r(u^n) \rightarrow \frac{-e^{2ik_rh_r} + 16e^{ik_rh_r} - 30 + 16e^{-ik_rh_r} - e^{-2ik_rh_r}}{12h_r^2} \hat{u}^n$$

$$= \frac{-4\sin^2\frac{k_rh_r}{2}\left(\sin^2\frac{k_rh_r}{2} + 3\right)}{3h_r^2} \hat{u}^n \tag{A3}$$

$$:= \frac{-\psi(k_r)}{h_r^2} \hat{u}^n.$$

After Fourier transform, Eq. (A1) is written as

$$\hat{u}^{n+1} - 2\hat{u}^n + \hat{u}^{n-1} = -2\delta\hat{u}^n, \tag{A4}$$

where

$$2\delta = \frac{v^2\Delta t^2}{J}\left[\frac{\psi(k_q)}{h_q^2}M_{qq} + \frac{\psi(k_r)}{h_r^2}M_{rr}\right], \tag{A5}$$

$\hat{u}$ is the spatial Fourier transform of the wavefield u, k_q, k_r is the wave number components, and i is the imaginary unit. Eq. (A4) is equivalent to the following form of matrix

$$\begin{bmatrix} \hat{u}^{n+1} \\ \hat{w}^{n+1} \end{bmatrix} = \begin{bmatrix} 2-2\delta & -1 \\ 1 & 0 \end{bmatrix}\begin{bmatrix} \hat{u}^n \\ \hat{w}^n \end{bmatrix}, \tag{A6}$$

where the augmented matrix on the right hand side of Eq. (A6) is denoted as **G**. When the spectral radius of **G** satisfies that $\rho(\mathbf{G}) \leq 1$, i.e., the moduli of all eigenvalues of **G** are not larger than 1, the finite difference scheme is stable. The eigenvalue λ of **G** satisfies the following characteristic equation

$$\lambda^2 - (2-2\delta)\lambda + 1 = 0. \tag{A7}$$

The roots of Eq. (A7) are

$$\lambda_{1,2} = 1 - \delta \pm \sqrt{-2\delta + \delta^2}. \tag{A8}$$

We have two cases:

1. $\delta^2 - 2\delta = \delta(\delta-2) > 0$. Then $\delta > 2$ and $\lambda_2 = 1-\delta-\sqrt{-2\delta+\delta^2} < -1$, or $\delta < 0$ and $\lambda_1 = 1 + |\delta| + \sqrt{2|\delta| + |\delta|^2} > 1$. Thus, the scheme is unstable.

2. $0 \leq \delta \leq 2$. Now $\delta^2 - 2\delta \leq 0$ and we get complex conjugated roots,

$$\lambda_{1,2} = 1 - \delta \pm i\sqrt{2\delta - \delta^2}, \tag{A9}$$

and

$$|\lambda_{1,2}|^2 = (1-\delta)^2 + 2\delta - \delta^2 = 1. \tag{A10}$$

We conclude that the scheme (A1) is stable for

$$0 \leq 2\delta = \frac{v^2\Delta t^2}{J}\left[\frac{\psi(k_q)}{h_q^2}M_{qq} + \frac{\psi(k_r)}{h_r^2}M_{rr}\right] \leq 4. \tag{A11}$$

Since $\frac{M_{qq}}{J} = q_x^2 + q_z^2 \geq 0$, $\frac{M_{rr}}{J} = r_x^2 + r_z^2 \geq 0$, $0 \leq \psi(k_q) \leq 16/3$, $0 \leq \psi(k_r) \leq 16/3$, so $2\delta \geq 0$. $\psi(k_q)$ and $\psi(k_r)$ take the maximum at $k_q = \frac{\pi}{h_q}$ and $k_r = \frac{\pi}{h_r}$ respectively, thus,

$$v^2\Delta t^2\left[\frac{\psi(k_q)}{h_q^2}\frac{M_{qq}}{J} + \frac{\psi(k_r)}{h_r^2}\frac{M_{rr}}{J}\right] \leq \frac{16}{3}v^2\Delta t^2\left[\frac{M_{qq}}{h_q^2 J} + \frac{M_{rr}}{h_r^2 J}\right] \leq 4. \tag{A12}$$

Hence, Eq. (9) is stable under the time step restriction

$$\Delta t \leq \frac{\sqrt{3}/2}{v\sqrt{\frac{1}{J}\left(\frac{M_{qq}}{h_q^2} + \frac{M_{rr}}{h_r^2}\right)}}. \tag{A13}$$

References

Berenger, J., 1994. A perfectly matched layer for the absorption of electromagnetic waves. J. Comput. Phys. 114, 185–200.

Carpenter, M.H., Nordström, J., Gottlieb, D., 1999. A stable and conservative interface treatment of arbitrary spatial accuracy. J. Comput. Phys. 148, 341–365.

Chen, H.M., Zhou, H., Lin, H., Wang, S.X., 2013. Application of perfectly matched layer for scalar arbitrarily wide-angle wave equations. Geophysics 78 (1), T29–T39.

Conti, C., Morandi, R., Spitaleri, R.M., 2005. An algebraic-elliptic algorithm for boundary orthogonal grid generation. Appl. Math. Comput. 162 (1), 15–27.

Del Rey Fernández, D.C., Hicken, J.E., Zingg, D.W., 2014. Review of summation-by-parts operators with simultaneous approximation terms for the numerical solution of partial differential equations. Comput. Fluids 95, 171–196.

Dovgilovich, L., Sofronov, I., 2015. High-accuracy finite-difference schemes for solving elastodynamic problems in curvilinear coordinates within multiblock approach. Appl. Numer. Math. 93, 176–194.

Duru, K., Dunham, E.M., 2016. Dynamic earthquake rupture simulations on nonplanar faults embedded in 3D geometrically complex, heterogeneous elastic solids. J. Comput. Phys. 305, 185–207.

Fornberg, B., 1987. The pseudospectral method: comparisons with finite differences for the elastic wave equation. Geophysics 52 (4), 483–501.

Guo, H.W., Wang, S.X., 2009. 2D wave equation pre-stack reverse-time migration for complex geology structures with rugged topography by finite-element method. 79th Annual International Meeting, SEG, Expanded Abstracts, pp. 2884–2888.

Guo, H.W., Wang, S.X., Guo, N.C., Chen, W., 2012. Wave equation simulation by finite-element method with perfectly matched layer. Adv. Mater. Res. 96–100.

Hicken, J.E., 2012. Output error estimation for summation-by-parts finite-difference schemes. J. Comput. Phys. 231 (9), 3828–3848.

Jeng, Y.N., Liou, Y.C., 1992. A new adaptive grid generation by elliptic equations with orthogonality at all of the boundaries. J. Sci. Comput. 7 (1), 63–80.

Kaul, U.K., 2003. New boundary constraints for elliptic systems used in grid generation problems. J. Comput. Phys. 189 (2), 476–492.

Kaul, U.K., 2010. Three-dimensional elliptic grid generation with fully automatic boundary constraints. J. Comput. Phys. 229 (17), 5966–5979.

Komatitsch, D., Tromp, J., 1999. Introduction to the spectral element method for three-dimensional seismic wave propagation. Geophys. J. Int. 139 (3), 806–822.

Kosloff, D., Kessler, D., Filho, A.Q., Tessmer, E., Behle, A., Strahilevitz, R., 1990. Solution of the equations of dynamic elasticity by a Chebychev spectral method. Geophysics 55 (6), 734–748.

Kozdon, J.E., Dunham, E.M., Nordstrom, J., 2013. Simulation of dynamic earthquake ruptures in complex geometries using high-order finite difference methods. J. Sci. Comput. 55 (1), 92–124.

Kress, W., 2003. A compact fourth order time discretization method for the wave equation. Technical Report 2003–041. Department of Information Technology, Uppsala University.

Lan, H.Q., Zhang, Z.J., 2011. Three-dimensional wave-field simulation in heterogeneous transversely isotropic medium with irregular free surface. Bull. Seismol. Soc. Am. 101 (3), 1354–1370.

Lan, H.Q., Zhang, Z.J., 2012. Seismic wavefield modeling in media with fluid-filled fractures and surface topography. Appl. Geophys. 9 (3), 301–312.

Lan, H.Q., Zhang, Z.J., Chen, J.Y., Liu, Y.S., 2014. Reverse time migration from irregular surface by flattening surface topography. Tectonophysics 627, 26–37.

Lan, H.Q., Chen, J.Y., Zhang, Z.J., Liu, Y.S., Zhao, J.G., Shi, R.Q., 2016. Application of a perfectly matched layer in seismic wavefield simulation with an irregular free surface. Geophys. Prospect. 64 (1), 112–128.

Liu, T., Hu, T.Y., Sen, M.K., Yang, J.H., Wang, R.Q., Wang, S.X., 2011. A hybrid scheme for seismic modelling based on Galerkin method. Geophys. J. Int. 186 (3), 1165–1178.

Mattsson, K., 2003. Summation-By-Parts Operators for High Order Finite Difference Methods. Uppsala University, Information Technology, Department of Scientific Computing (PhD Thesis).

Mufti, I.R., 1990. Large-scale three-dimensional seismic models and their interpretive significance. Geophysics 55 (9), 1166–1182.

Nordstrom, J., Carpenter, M.H., 1998. Boundary and Interface Conditions for High Order Finite Difference Methods Applied to the Euler and Navier-Stokes Equations. National Aeronautics and Space Administration, Washington, D.C. (NASA Contractor Report-207681).

Petersson, N.A., Sjögreen, B., 2009. An energy absorbing far-field boundary condition for the elastic wave equation. Commun. Comput. Phys. 6 (3), 483–508.

Petersson, N.A., Sjögreen, B., 2010. Stable grid refinement and singular source discretization for seismic wave simulations. Commun. Comput. Phys. 8 (5), 1074–1110.

Petersson, N.A., Sjögreen, B., 2014. Super-grid modeling of the elastic wave equation in semibounded domains. Commun. Comput. Phys. 16 (4), 913–955.

Petersson, N.A., Sjögreen, B., 2015. Wave propagation in anisotropic elastic materials and curvilinear coordinates using a summation-by-parts finite difference method. J. Comput. Phys. 299, 820–841.

Rao, Y., Wang, Y.H., 2013. Seismic waveform simulation with pseudo-orthogonal grids for irregular topographic models. Geophys. J. Int. 194 (3), 1778–1788.

Sherer, S.E., Scott, J.N., 2005. High-order compact finite-difference methods on general overset grids. J. Comput. Phys. 210 (2), 459–496.

Sjögreen, B., 2012. High order finite difference and finite volume methods for advection on the sphere. J. Sci. Comput. 51 (3), 703–732.

Sjögreen, B., Petersson, N.A., 2012. A fourth order accurate finite difference scheme for the elastic wave equation in second order formulation. J. Sci. Comput. 52 (1), 17–48.

Sjögreen, B., Petersson, N.A., 2014. Source estimation by full wave form inversion. J. Sci. Comput. 59 (1), 247–276.

Strand, B., 1994. Summation by parts for finite difference approximations for d/dx. J. Comput. Phys. 110, 47–67.

Tarrass, I., Giraud, L., Thore, P., 2011. New curvilinear scheme for elastic wave propagation in presence of curved topography. Geophys. Prospect. 59 (5), 889–906.

Thompson, J.F., Thames, F.C., Mastin, C.W., 1977a. Boundary-Fitted Curvilinear Coordinate Systems for Solution of Partial Differential Equations on Fields Containing Any Number of Arbitrary Two-Dimensional Bodies. National Aeronautics and Space Administration, Washington, D.C. (NASA Contractor Report-2729).

Thompson, J.F., Thames, F.C., Mastin, C.W., 1977b. TOMCAT-A code for numerical generation of boundary-fitted curvilinear coordinate systems on fields containing any number of arbitrary two-dimensional bodies. J. Comput. Phys. 24 (3), 274–302.

Thompson, J.F., Warsi, Z.U.A., Mastin, C.W., 1985. Numerical Grid Generation: Foundations and Applications. Elsevier North-Holland (ISBN 044400985×).

Wang, Y., Zhou, H., Chen, H.M., Sheng, S.B., Yuan, S.Y., 2015. Acoustic reverse time migration and perfectly matched layer in boundary-conforming grids by elliptic method. J. Appl. Geophys. 122, 53–61.

Wei, W.L., Wang, D.Y., Liu, Y.L., 2000. Some improvement on technique of orthogonal curvilinear grid generation. J. Wuhan Univ. Hydraul. Electr. Eng. 33 (2), 40–42 (in Chinese).

Yang, D.H., Tong, P., Deng, X.Y., 2012. A central difference method with low numerical dispersion for solving the scalar wave equation. Geophys. Prospect. 60 (5), 885–905.

Yuan, S.Y., Wang, S.X., Sun, W.J., Miao, L.N., Li, Z.H., 2014. Perfectly matched layer on curvilinear grid for the second-order seismic acoustic wave equation. Explor. Geophys. 45 (2), 94–104.

Zhang, Y., Sun, J., 2009. Practical issues of reverse time migration: true amplitude gathers, noise removal and harmonic-source encoding. First Break 27 (1), 53–60.